

# A Novel 6-axis Force/Torque Sensor Using Inductance Sensors

Hyun-Bin Kim and Kyung-Soo Kim, *Member, IEEE*,

**Abstract**—This paper presents a novel six-axis force/torque (F/T) sensor based on inductive sensing technology. Unlike conventional strain gauge-based sensors that require direct contact and external amplification, the proposed sensor utilizes non-contact inductive measurements to estimate force via displacement of a conductive target. A compact, fully integrated architecture is achieved by incorporating a CAN-FD based signal processing module directly onto the PCB, enabling high-speed data acquisition at up to 4 kHz without external DAQ systems. The sensing mechanism is modeled and calibrated through a rational function fitting approach, which demonstrated superior performance in terms of root mean square error (RMSE), coefficient of determination ( $R^2$ ), and linearity error compared to other nonlinear models. Static and repeatability experiments validate the sensor's accuracy, achieving a resolution of 0.03 N and quantization levels exceeding 55,000 steps, surpassing that of commercial sensors. The sensor also exhibits low crosstalk, high sensitivity, and robust noise characteristics. Its performance and structure make it suitable for precision robotic applications, especially in scenarios where compactness, non-contact operation, and integrated processing are essential.

**Index Terms**—Force/torque sensor, inductive sensor, non-contact measurement

## I. INTRODUCTION

RECENT years have witnessed rapid advancements in various robotics domains—such as collaborative robots (co-bots), quadruped robots, and humanoids [1]–[6]. Among these, collaborative robots (co-bots) in particular require precise force control to ensure safe and reliable interaction with human operators, leading to a sharp increase in the demand for six-axis force/torque (F/T) sensors. Currently, the majority of commercially available six-axis sensors are based on strain-gauge technology, which is widely adopted due to its proven reliability and broad applicability. However, strain-gauge-based sensors [7]–[9] are inherently limited by their high production costs and finite durability. These sensors typically operate via direct contact, using adhesives such as silicone to bond strain-gauges onto elastomeric substrates. This structure is vulnerable to degradation under repeated loading and external impacts, raising concerns about long-term reliability and durability. In addition, these sensors often require dedicated data acquisition

(DAQ) equipment. Consequently, when multiple sensors are employed, multiple DAQ units are also needed, which poses practical limitations in the development of complex robotic systems such as multi-jointed robots.

To address these limitations in cost and robustness, non-contact sensing technologies for F/T measurement have garnered increasing attention. A representative example is the capacitive sensing approach, which indirectly estimates applied force by monitoring changes in capacitance between electrodes and a grounded plate [10]–[12]. Capacitive sensors are valued for their low production costs and structural simplicity, making them suitable for applications such as robotic hands and compact surgical F/T sensors [13], [14]. Their compact form factor and flexibility in design further enhance their applicability in embedded robotic systems.

In addition, optical sensing techniques have also been explored extensively [15]–[17]. These include distance measurement via photocouplers [18]–[20] and strain detection using fiber Bragg grating (FBG) sensors [21]. Photocoupler-based systems offer advantages in miniaturization and circuit simplicity, resulting in reduced part count and lower manufacturing cost. Conversely, FBG-based sensors provide exceptional precision and sensitivity, but require dedicated optical transducers and analysis equipment, which increase the system's bulk and complexity. Moreover, optical sensors are generally more susceptible to environmental temperature variations compared to capacitive approaches, necessitating additional compensation mechanisms [22].

While these non-contact technologies each have unique advantages, they still face challenges related to cost-effectiveness, durability, compact integration, and temperature stability. In response, this study proposes a novel six-axis F/T sensor that leverages inductance variation for force detection. Inspired by the operational principle of metal detectors, the proposed sensor uses changes in inductance-caused by the displacement of nearby metallic elements within a magnetic field generated by coils to precisely infer force. The inductive sensing approach offers robust resistance to mechanical impact, stable performance under temperature variation, and the advantage of non-contact operation. In terms of temperature sensitivity, capacitive sensors are significantly affected due to the strong dependence of permittivity on temperature. In contrast, although inductive sensors can exhibit variations in magnetic permeability with respect to temperature—particularly in magnetic materials—these changes are generally smaller and more stable, resulting in relatively lower temperature sensitivity.

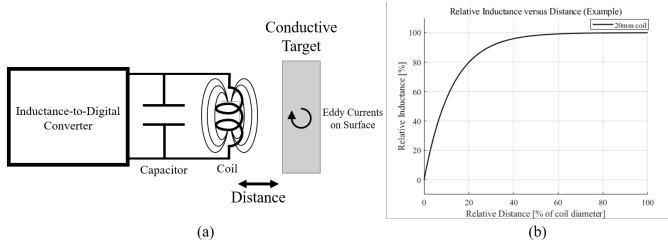


Fig. 1. Principle of the proposed sensor (a). Inductance-to-digital converter with conductive target (b). Relative Inductance versus distance between coil and conductive target

This paper systematically presents the design methodology, fabrication process, performance evaluation, and comparative analysis of the proposed inductive sensor against existing commercial alternatives.

### A. Contribution

The key contributions of this study are summarized as follows:

- **Introduction of a non-contact inductive sensing method:** A novel measurement principle based on inductance variation is proposed to overcome the limitations of conventional strain-gauge and capacitive sensors. The proposed approach simultaneously achieves cost-efficiency and enhanced durability while offering improved resilience to environmental disturbances.
- **Fully integrated Printed Circuit Board(PCB)-based sensor architecture:** The sensor is designed using a PCB-only structure, eliminating the need for complex mechanical assembly or additional discrete components. This significantly simplifies the manufacturing process and enhances consistency and reliability in large-scale production.
- **High-resolution force detection performance:** By precisely modeling and calibrating the coil inductance, the proposed sensor achieves a resolution more than twice that of conventional strain-gauge sensors, reaching approximately 0.03 N. Experimental validation confirms its applicability in precision-sensitive robotic and industrial tasks.
- **Compact integration of onboard signal processing:** In contrast to traditional sensors that rely on external signal processing units, the proposed design integrates a CAN-based signal processing module directly into the PCB. This compact integration eliminates the need for external DAQ hardware, thereby reducing wiring complexity and enhancing overall system flexibility and deployability.

## II. DESIGN OF THE PROPOSED SENSOR

### A. Principle of the Proposed Sensor

The operating principle of the proposed sensor is fundamentally based on the same principle as that of a metal detector. As illustrated in Fig.1(a), the sensor measures the resonant frequency of a system composed of a capacitor and a coil, where the resonant frequency is given by  $f_0 = 1/2\pi\sqrt{LC}$ .

When a metallic object approaches the vicinity of the inductor, the surrounding magnetic field is disturbed, leading to eddy current losses. As a result, the inductance  $L$  decreases. An inductance-to-digital converter (LDC) detects this change in frequency with high precision and digitizes the measurement for output. As shown in Fig.1(b), when the distance between the coil and the metallic object reaches a certain range relative to the coil diameter, the relative inductance changes noticeably. This principle enables the estimation of the distance between the coil and the metallic object. By exploiting this phenomenon, when a force is applied to an elastomer, causing a slight deformation, the resulting distance change can be detected and subsequently back-calculated to estimate the applied force.

$$D_{in} = D_{out} - (2N + 1)s - (2N - 1)w \quad (1)$$

$D_{in}$  denotes the inner diameter of the coil, while  $D_{out}$  represents the outer diameter. Here,  $N$  indicates the number of turns,  $s$  is the spacing between adjacent traces, and  $w$  denotes the width of a single trace.

$$D_{avg} = \left(1 + \frac{4}{\pi} \left(\frac{d_L}{D_{out}} - 1\right)\right) \cdot \frac{D_{in} + D_{out}}{2} \quad (2)$$

The average diameter  $D_{avg}$  is calculated using the above expression, where  $d_L$  denotes the diameter measured at the center of the outermost trace. Instead of a simple arithmetic mean, a correction factor  $\left(1 + \frac{4}{\pi} \left(\frac{d_L}{D_{out}} - 1\right)\right)$  is introduced to account for the physical distribution of the coil windings.

$$\alpha = \frac{D_{out} - D_{in}}{D_{out} + D_{in}} \quad (3)$$

The geometric parameter  $\alpha$  quantifies the ratio of the coil thickness to its overall size. This parameter reflects how thickly the coil is wound and influences the inductance calculation.

$$L_{layer} = \frac{\mu_0}{2} \cdot N^2 \cdot D_{avg} \cdot \left[ \ln \left( \frac{2.46}{\alpha} \right) + 0.2\alpha^2 \right] \quad (4)$$

Since the PCB typically consists of multiple layers, the self-inductance  $L_{layer}$  of a single layer is computed. It is determined by the permeability of free space  $\mu_0$ , the number of turns  $N$ , and the average diameter  $D_{avg}$ . The geometric parameter  $\alpha$  is incorporated through a logarithmic and polynomial adjustment to more accurately reflect the coil's geometry.

$$k(h) = \frac{1}{0.184h^3 - 0.525h^2 + 1.038h + 1.001} \quad (5)$$

Here,  $h$  denotes the normalized distance between layers. The coupling factor  $k(h)$  characterizes the magnetic coupling strength between adjacent layers and is essential for calculating mutual inductance between different layers.

$$L_{total} = \left( 2 \sum_{i=1}^{M-1} k_i + M \right) \cdot L_{layer} \quad (6)$$

The total inductance  $L_{total}$  in the absence of a metallic target is computed by combining the self-inductance and mutual

inductance contributions.  $M$  represents the number of layers, with  $M \cdot L_{\text{layer}}$  accounting for the self-inductance and the summation term capturing the interlayer coupling.

$$f_{\text{res}} = \frac{1}{2\pi\sqrt{L_{\text{total}}(C + C_{\text{par}})}} \quad (7)$$

The resonant frequency  $f_{\text{res}}$  of the LC circuit without a metallic target is calculated using the total inductance  $L_{\text{total}}$  and the capacitance  $C$  combined with the parasitic capacitance  $C_{\text{par}}$ . In this study, a parasitic capacitance of 4 pF is assumed based on the circuit layout.

$$\Delta L = L_{\text{total}} - L' = L_{\text{layer}} \cdot [(2\sum k_i^{\text{target}} + M) - (2\sum k_i + M)] \quad (8)$$

When a conductive target interacts with the coil, the inductance decreases. The proximity of the target modifies the coupling coefficients  $k_i^{\text{target}}$  between layers, leading to a change in total inductance  $\Delta L$ . This variation can be correlated to external force applied to the elastomer. [23]–[25]

The LDC measures the resonant frequency  $f'_{\text{res}} = \frac{1}{2\pi\sqrt{L'_{\text{total}}(C + C_{\text{par}})}}$  to detect changes in inductance. As the LDC measures a value inversely proportional to the frequency, the raw digital output is effectively proportional to  $\sqrt{L}$ .

### B. Elastomer and Printed Circuit Board Design

The elastomer structure adopts the widely used T-beam design, which is one of the most common configurations in six-axis F/T sensors employing strain-gauges. As illustrated in Fig.2(a), three T-beams are arranged at 120-degree intervals within the elastomer. The corresponding geometric parameters  $l_1$ ,  $l_2$ ,  $b_1$ ,  $b_2$ , and  $h$  are defined as listed in Table I. The structure is designed to withstand a minimum of 800 N of force and 27 N·m of torque. The sensing PCB of the proposed sensor,

TABLE I  
VALUE OF T-BEAM

Variable	$l_1$	$l_2$	$b_1$	$b_2$	$h$
Value (mm)	21.5	31.7	4	0.5	7

as illustrated in Fig. 2(b), comprises two distinct types of coils: vertical sensing coils and horizontal sensing coils. The vertical sensing coils are primarily utilized for measuring the torque components  $T_x$ ,  $T_y$ , and the axial force  $F_z$ , whereas the horizontal sensing coils are designed to detect the lateral forces  $F_x$ ,  $F_y$ , and the torsional torque  $T_z$ .

The vertical sensing coils are implemented with 18 turns distributed across three layers. Each trace has a width of 4 mil and an inter-trace spacing of 4 mil, with a copper thickness of 1 oz and a coil diameter of 10 mm. The spacing between the first and second layers is 59 mil, while that between the second and third layers is 5.9 mil.

The horizontal sensing coils consist of 10 turns across four layers, with an overall height of 4.7 mm and a width of 13 mm. The spacing between the third and fourth layers is also set to 5.9 mil.

Fig. 2(c) shows the signal processing printed circuit board, which incorporates the LDC1614 chip by Texas Instruments.

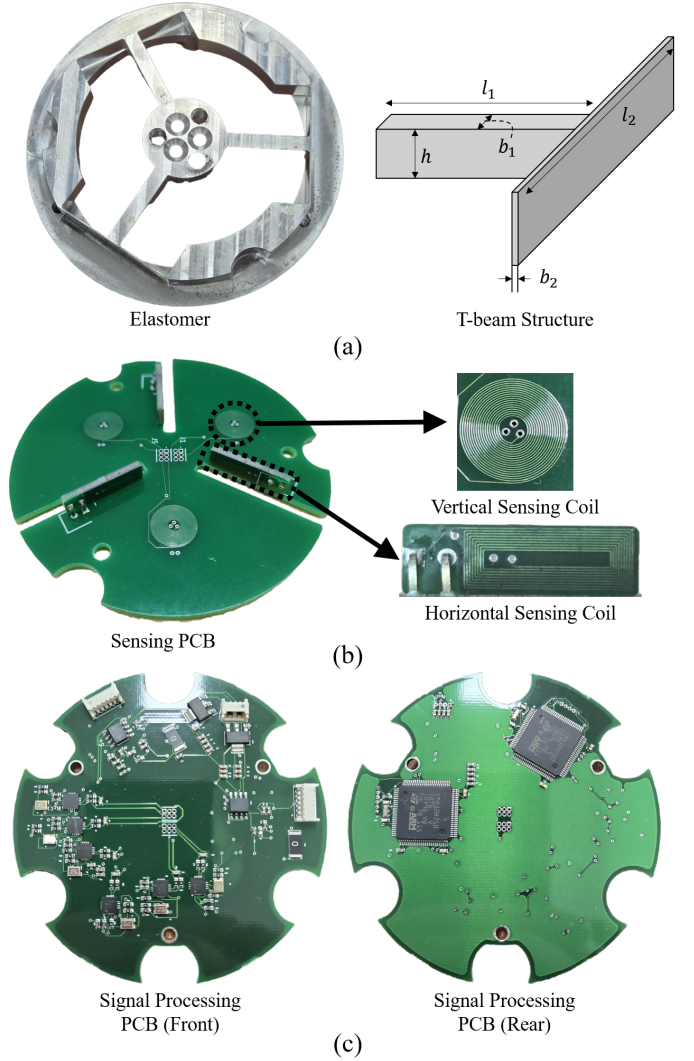


Fig. 2. Elastomer and printed circuit board design (a) Elastomer and T-beam structure (b) Sensing PCB with vertical sensing coil and horizontal sensing coil (c) Signal processing PCB design

A high-performance STM32H750 microcontroller is integrated into the board, enabling direct communication via the CAN protocol. CAN-FD communication, supporting data rates up to 5 Mbps, is utilized for high-speed data transmission.

To support high-frequency sampling, each sensing coil is connected to a dedicated LDC1614 channel, allowing for parallel and rapid inductance measurements. The system operates with a 5 V input voltage and provides four external connections: power input, ground, CAN High, and CAN Low. This architecture enables a compact and fully integrated sensor module, well-suited for deployment in embedded robotic systems.

### C. Sensor Fabrication

The proposed sensor consists of five machined metal components and two PCBs. All metallic parts are fabricated using AL7075-T6, an aluminum alloy known for its relatively low

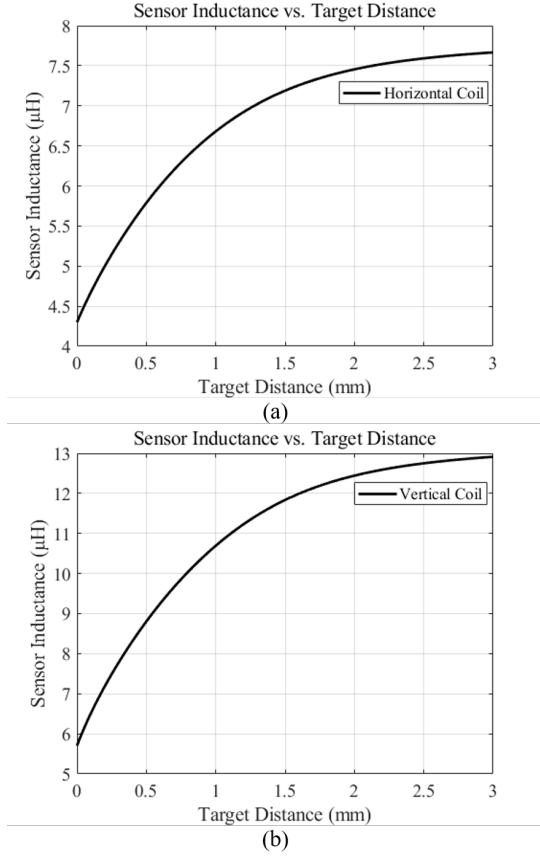


Fig. 3. Calculated graph of coils' inductance and conductive target distance (a) Horizontal coil (b) Vertical coil

hysteresis compared to other aluminum grades. As illustrated in Fig. 4, the assembly process follows a bottom-up structure.

As shown in Fig. 4, the sensor consists of five metallic components and two PCB parts. All components are fastened using bolts in combination with a threadlocker adhesive. At the base of the sensor, the signal processing PCB is enclosed within the bottom part. A support structure is mounted above the base to secure the sensing PCB in position. A metal plate is placed above the sensing PCB, serving as the inductive target for distance measurements by the coils. This metal plate is mechanically coupled to the elastomer, which is clamped between the support part and the bottom part using bolts, thereby ensuring structural integrity.

The top part functions as the interface through which external forces are applied to the sensor. Although copper offers higher sensitivity due to its greater conductivity, aluminum is selected for the metal plate to maintain sufficient performance while ensuring material consistency and manufacturability across the structure.

Table II summarizes the mechanical specifications of the proposed sensor. The sensor has a diameter of 85 mm and a height of 36 mm, and it operates at a sampling rate of approximately 4 kHz, which corresponds to the maximum rate supported by the LDC1614 IC (4.08 kHz). Including the PCB, the total weight of the sensor is 280 g.

As also shown in Table II, the sensor is designed to

TABLE II  
MECHANICAL SPECIFICATION OF THE PROTOTYPE SENSOR

	Value	Unit
Diameter	85	mm
Height	36	mm
Material	AL7075-T6	
Input force range ( $F_x$ and $F_y$ )	$\pm 890$	N
Input force range ( $F_z$ )	$\pm 1,435$	N
Input torque range ( $T_x, T_y$ )	$\pm 27$	N·m
Input torque range ( $T_z$ )	$\pm 45$	N·m
Sampling frequency	4	kHz
Weight	280	g

measure forces in the range of 890 N to 1435 N, and torques ranging from 27 N·m to 45 N·m. Owing to the symmetric configuration of the T-beam structure, the sensor demonstrates nearly identical force responses along the  $x$ - and  $y$ -axes. Likewise, the torque responses about the  $x$ - and  $y$ -axes exhibit similar characteristics, ensuring consistent performance in planar loading conditions.

### III. SENSOR EVALUATION

The performance of the proposed sensor was evaluated by comparison with a calibrated commercial six-axis F/T sensor, the MINI-85 SI-1900-80 model from ATI Industrial Automation. Prior to evaluation, a calibration procedure was required.

#### A. Calibration

For calibration, a widely adopted method from the literature was employed, wherein direct force application is used to relate known inputs to sensor outputs. As illustrated in Fig. 5, the proposed sensor was rigidly connected to the reference sensor via a custom-designed connection jig, and external forces were applied manually using a handle.

Each sensing coil in the proposed sensor produces a digital output via an inductance-to-digital converter, which reflects the square root of the inductance value, i.e.,  $\sqrt{L}$ . Since the inductance  $L$  exhibits a nonlinear relationship with the distance between the sensing coil and the target metal plate, constructing a conventional linear calibration matrix results in reduced accuracy. Therefore, a more robust nonlinear calibration approach is necessary to accurately map sensor outputs to the corresponding F/T.

$$F = \mathbf{A}y, \quad y = \begin{bmatrix} y_1 \\ y_2 \\ y_3 \\ y_4 \\ y_5 \\ y_6 \\ 1 \end{bmatrix} \quad (9)$$

$$y = f(x_{\text{raw}}) \quad (10)$$

Here,  $F$  denotes the F/T vector, and  $y$  represents the deformation. The variable  $x_{\text{raw}}$  refers to the raw data output from the LDC1614, and the function  $f$  describes the relationship between  $x_{\text{raw}}$  and  $y$ . Since the LDC1614 output is proportional

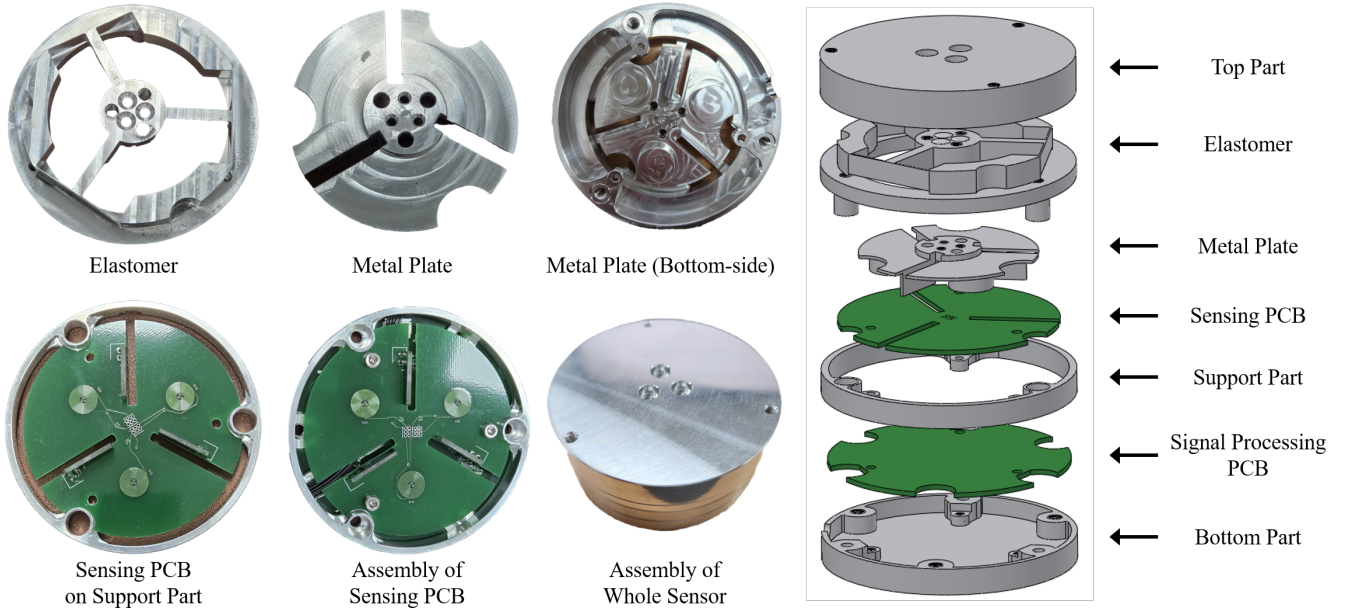


Fig. 4. Components of the proposed sensor; Five metallic components: Top part, elastomer, metal plate, support part and bottom part, two PCB components: Sensing PCB and Signal Processing PCB.

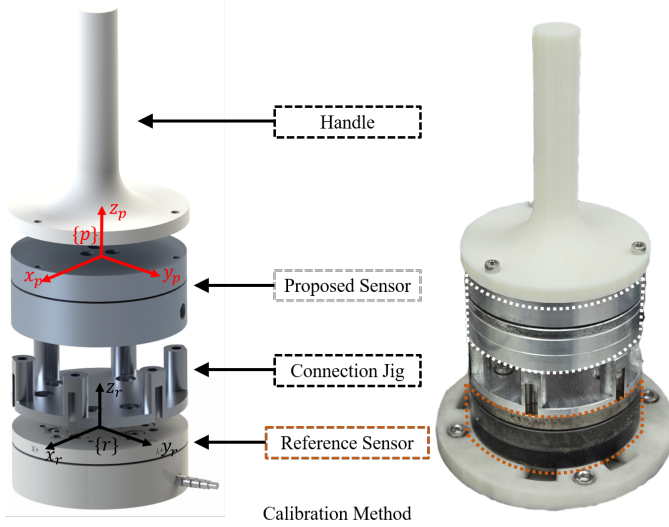


Fig. 5. Calibration method with direct connecting along the  $z$ -axis with connection jig; F/T applied via handle for calibration.

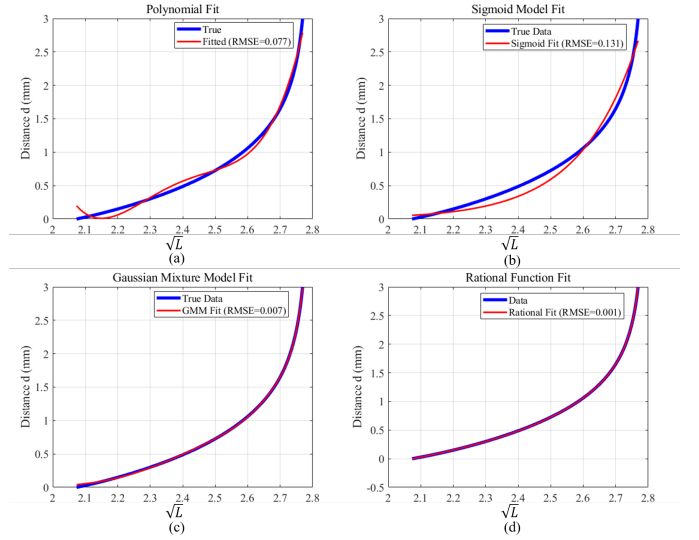


Fig. 6. Fitting result of each method: (a) Polynomial fitting; (b) Sigmoid model fitting; (c) Gaussian mixture model fitting; (d) Rational function fitting.

to frequency, it is also proportional to  $\sqrt{L}$ . The matrix  $\mathbf{A}$  is a  $6 \times 7$  calibration matrix that maps the deformation to the corresponding F/T values.

Since the LDC1614 measures the square root of inductance  $\sqrt{L}$ , the relationship between  $\sqrt{L}$  and the target distance was used for calibration. Fig. 6 compares the results of polynomial fitting, sigmoid model fitting, Gaussian mixture model fitting, and rational function fitting. Each model includes five or six parameters, and their respective formulations are given as follows.

$$y = a_4x^4 + a_3x^3 + a_2x^2 + a_1x + a_0 \quad (11)$$

Here,  $x$  denotes  $\sqrt{L}$  and  $y$  represents the target distance  $d$ . The coefficients  $a_n$  correspond to the  $n$ -th order polynomial terms.

$$y = b_1/(1 + \exp(-b_2(x - b_3))) + b_4/(1 + \exp(-b_5(x - b_6))) \quad (12)$$

Similarly, in the sigmoid model,  $x$  denotes  $\sqrt{L}$  and  $y$  represents the target distance  $d$ . The fitting result using the sigmoid



function is shown in Fig. 6(b), where the root mean square error (RMSE) was found to be 0.131. Each parameter  $b_n$  represents the  $n$ -th coefficient of the sigmoid model.

$$y = c_1 \exp(-(x - c_2)^2 / (2c_3^2)) + c_4 \exp(-(x - c_5)^2 / (2c_6^2)) \quad (13)$$

In the same manner, a commonly used nonlinear model fitting technique, the Gaussian mixture model, is formulated as follows. The coefficients  $c_n$  denote the parameters of the Gaussian mixture model, with a total of six parameters. As shown in Fig. 6(c), this model yielded a relatively lower RMSE of 0.007 compared to the previous two models.

$$y = (d_1 x^2 + d_2 x + d_3) / (d_4 x^2 + d_5 x + 1) \quad (14)$$

Finally, the rational function fitting model is presented. The coefficients  $d_n$  represent the parameters of the rational function. As illustrated in Fig. 6(d), the rational function exhibits a significantly lower RMSE of 0.001 compared to the other models. This suggests that the structural nature of  $\sqrt{L}$  is particularly well-suited to rational function fitting, and thus, this model was employed for calibration. To simultaneously determine the rational function coefficients and the calibration matrix, an optimization-based approach was adopted. Specifically, MATLAB's `lsqnonlin` function was utilized for the calibration procedure.

TABLE III  
COMPARISON OF EACH FITTING FUNCTION

Model	# Parameters	RMSE	$R^2$	Linearity Error (%)
Polynomial function	5	0.0488	0.9968	4.73
Sigmoid function	6	0.1307	0.9774	11.30
Gaussian model	6	0.1404	0.9739	12.04
Rational function	5	<b>0.0009</b>	<b>1.0000</b>	<b>0.11</b>

To quantitatively evaluate each fitting model, three key metrics were computed: RMSE, coefficient of determination ( $R^2$ ), and linearity error (maximum deviation as a percentage of full scale). Table III summarizes the results.

Among the compared models, the rational function achieved the lowest RMSE (0.0009), the highest  $R^2$  score (1.0000), and the smallest linearity error (0.11%). Notably, it also required only five parameters, whereas other nonlinear models, such as the sigmoid function, used six. These results suggest that the rational model not only provides the best fit but also demonstrates superior generalizability and robustness.

## B. Evaluation

The sensor performance was evaluated using a static force measurement approach, which is commonly adopted in previous studies [18]. Two metrics were used to quantify the performance: RMSE of the time response, and percentage error. The percentage error was computed as the full-scale error, defined as the difference between the proposed sensor and the reference sensor divided by the full measurement range of the proposed sensor.

Each measurement was conducted for 100 seconds per axis. During this period, forces were repeatedly applied multiple times along each axis, effectively serving as a repeatability test in addition to static evaluation.

Fig. 7 presents the results for all six axes, showing that the proposed sensor exhibits a close match with the reference sensor across all directions. Both sensors were sampled at 1 kHz, and the reference sensor employed an 838 Hz low-pass filter. During the experiments, the reference sensor transmitted data via Ethernet UDP communication, while the proposed sensor utilized CAN communication. All experiments were conducted using Simulink Desktop Real-Time. Notably, the proposed sensor did not apply any low-pass filtering during the measurements.

TABLE IV  
FULL-SCALE ERROR AND RMSE ANALYSIS

	Percentage Error (%)			RMS Error (N, N-m)
	Mean	Std	Max	
$F_x$	0.0119	0.0154	0.151	0.310
$F_y$	0.0125	0.0161	0.0916	0.318
$F_z$	0.102	0.137	0.641	3.92
$T_x$	0.0346	0.0452	0.209	0.0244
$T_y$	0.0891	0.120	0.749	0.0648
$T_z$	0.00887	0.0110	0.0728	0.00989

Table IV summarizes the error analysis of the proposed sensor. The maximum percentage error observed in force measurements was 0.64% in the  $F_z$  direction, while the highest error in torque measurement was 0.75% in the  $M_y$  direction. Since most commercial six-axis F/T sensors specify a full-scale percentage error of approximately 1% per axis, the proposed sensor can be considered to meet the standard performance requirements of commercial-grade systems.

In addition, a resolution evaluation was conducted to further assess the performance of the proposed sensor. The resolution was compared against two widely used commercial sensors: a strain-gauge-based sensor (MINI-85 by ATI Industrial Automation [7]), which shares a similar elastomer structure, and a capacitive sensor developed by AIDIN ROBOTICS [26].

To quantify resolution, the standard deviation of each axis was calculated over a 10-second interval for both the MINI-85 and the proposed sensor. The computed standard deviations were then used to determine the resolution for each axis. The detailed results are summarized in Table V.

TABLE V  
COMPARISON OF STANDARD DEVIATION BETWEEN COMMERCIAL SENSOR AND PROPOSED SENSOR

	$F_x \& F_y$	$F_z$	$T_x \& T_y$	$T_z$
Company(A)	0.116	0.175	0.00570	0.00332
Proposed Sensor	0.0120	0.0386	0.00151	0.000574

Using this method, the resolution of the proposed sensor was determined, and the results are presented in Table VI. The outcomes are reported in terms of resolution (in N and N-m) and the corresponding number of quantization levels.

As shown in Table VI, the proposed sensor demonstrates a resolution of approximately 0.035 N for the  $x$ - and  $y$ -axis forces, which is roughly nine times finer than that of the

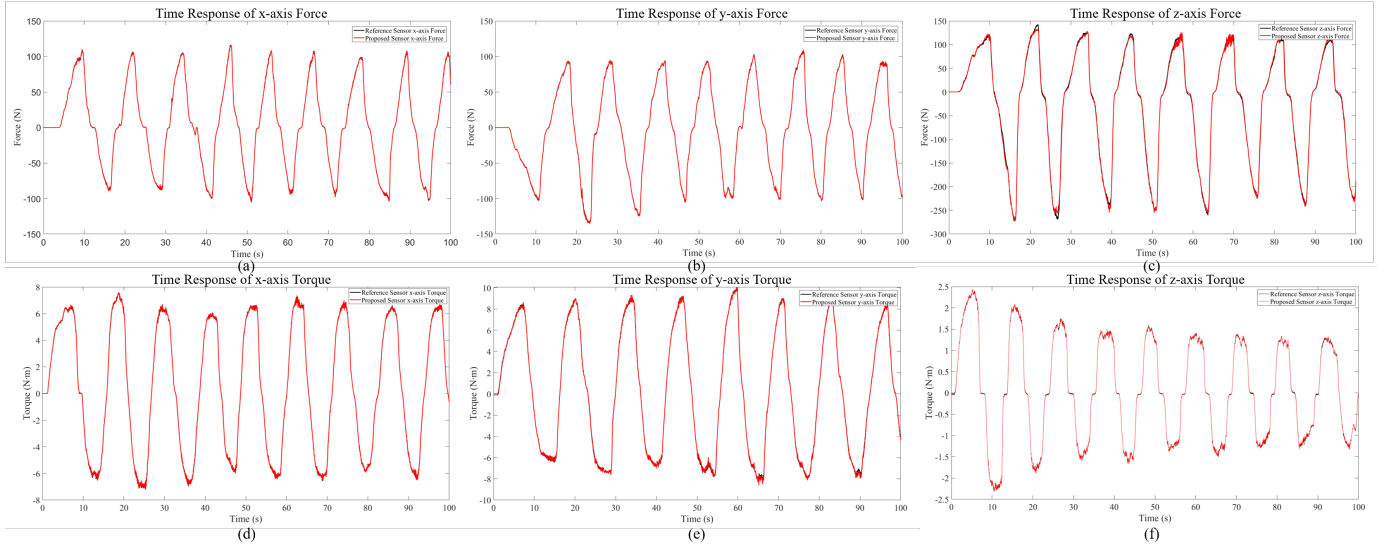


Fig. 7. Static time response evaluation of each axis F/T : (a) x-axis force; (b) y-axis force; (c) z-axis force; (d) x-axis torque; (e) y-axis torque; (f) z-axis torque.

TABLE VI  
COMPARISON OF SENSOR RESOLUTION BETWEEN COMMERCIAL SENSORS AND PROPOSED SENSOR

Resolution	$F_x & F_y$ (N)	$F_z$ (N)	$T_x & T_y$ (N·m)	$T_z$ (N·m)
Company(A)	0.321	0.429	0.0134	0.00936
Company(B)	0.150	0.150	0.0150	0.0150
Proposed Sensor	<b>0.0347</b>	<b>0.0945</b>	<b>0.00365</b>	<b>0.00163</b>
Quantization Levels	$F_x & F_y$	$F_z$	$T_x & T_y$	$T_z$
Company(A)	11822	17733	11968	17097
Company(B)	4000	4000	3333	3333
Proposed Sensor	<b>51312</b>	<b>30370</b>	<b>14810</b>	<b>55351</b>

reference sensor. Additionally, the resolution in the  $T_z$  torque is as low as 1.6 mN·m, indicating high sensitivity in torque measurements as well.

The quantization level, defined as the ratio of the full-scale range to the resolution, serves as an effective indicator of how finely the sensor can distinguish force or torque inputs. The proposed sensor achieves up to 55,351 quantization steps, which is more than twice the granularity offered by conventional sensing methods.

TABLE VII  
CROSSTALK PERCENTAGE ERROR MATRIX (%)

	$F_x$	$F_y$	$F_z$	$T_x$	$T_y$	$T_z$
$F_x$	100.	0.193	0.152	0.0248	0.153	0.0279
$F_y$	0.0907	100.	0.0773	0.0642	0.00533	0.0102
$F_z$	0.236	0.128	100.	0.0161	0.0146	0.0345
$T_x$	0.175	0.301	0.195	100.	0.00125	0.150
$T_y$	0.596	0.719	0.385	0.152	100.	0.122
$T_z$	0.0654	0.201	0.0555	0.0457	0.00600	100.

Crosstalk was also evaluated by applying force to individual axes as well as simultaneously to multiple axes. The crosstalk values are expressed as a percentage, representing the full-

scale ratio based on the sensor ranges listed in Table II. For example, the x-axis force has a range of 890 N, and therefore the full-scale reference value used for the calculation was 1780 N.

#### IV. DISCUSSION AND CONCLUSION

The primary contribution of this work lies in the novel inductive sensing structure, mechanical integration, and system-level validation. While nonlinear fitting techniques were used to improve calibration accuracy, the focus of the study is not on the calibration algorithm itself but on demonstrating the sensor's overall performance and practical applicability.

The proposed calibration process was validated through extensive static and repeatability experiments, showing consistent results with low RMSE and percentage error across all axes. These results indicate that the system operates robustly within the expected sensing range, even without explicit noise sensitivity analysis.

Among the evaluated fitting models, the rational function achieved the lowest RMSE despite using only five parameters, whereas other models, such as the Gaussian mixture and sigmoid models, employed six parameters. This suggests that the rational model provides a more efficient and generalizable representation of the underlying nonlinearity. Therefore, the choice of rational fitting is justified not only by accuracy but also by model simplicity and robustness against overfitting.

Fig. 8 presents an enlarged view of the static force response. Fig. 8(a) shows the x-axis force, (b) shows the y-axis force, and (c) depicts the z-axis torque. In each plot, the red line represents the proposed sensor, while the black line corresponds to the reference sensor. A comparison of the two responses reveals that the proposed sensor exhibits significantly lower noise levels.

In terms of performance, the proposed sensor demonstrates superior resolution, achieving up to four times higher quantiza-

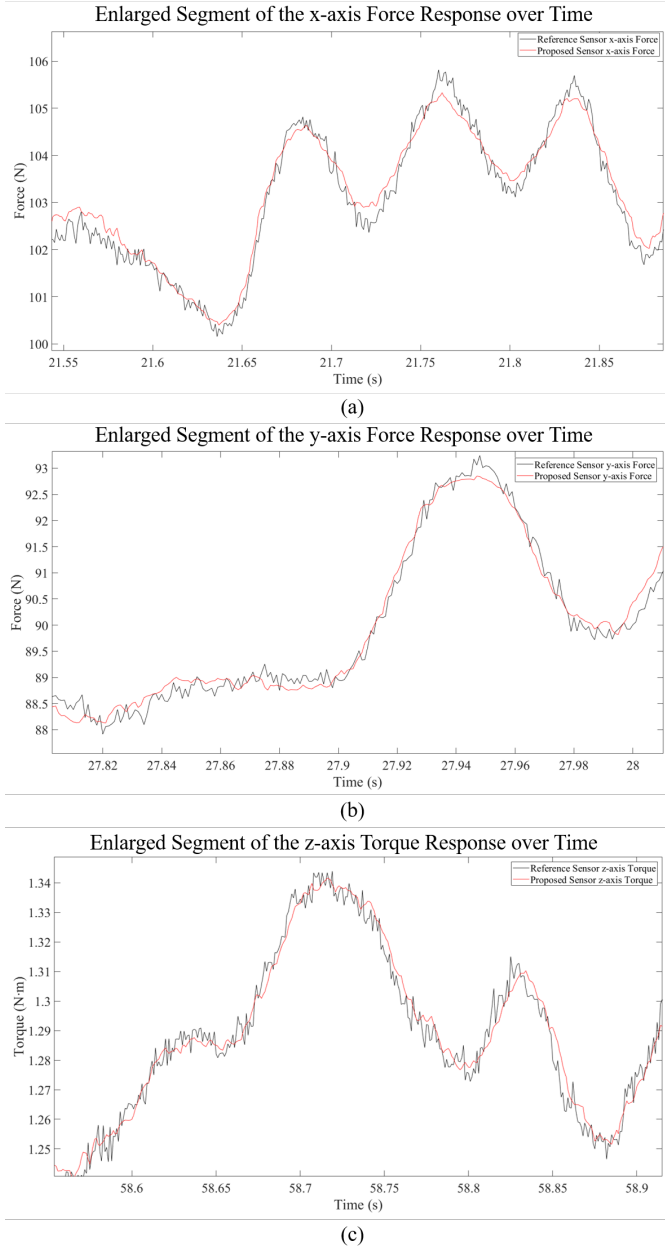


Fig. 8. Magnified static F/T responses for evaluation: (a) Force along  $x$ -axis ( $F_x$ ); (b) Force along  $y$ -axis ( $F_y$ ); (c) Torque about  $z$ -axis ( $M_z$ ).

tion levels compared to a commercial sensor. Most commercial sensors rely on external DAQ units and, in the case of strain-gauge-based systems, require both a Wheatstone bridge and an amplifier to detect strain variations. This amplification process inherently introduces noise, and achieving high resolution typically necessitates extensive filtering.

In contrast, the proposed sensor does not require amplification, as it measures inductance variation directly. This structural advantage inherently results in lower noise. Furthermore, the system supports a maximum sampling rate of approximately 4 kHz, which is sufficiently fast for dynamic measurements. Many commercial sensors operate at sampling rates around 200 Hz, indicating that the proposed sensor also

offers benefits in terms of data acquisition speed. Additionally, due to its non-contact measurement principle, the proposed sensor provides improved robustness against impact and long-duration loading, unlike traditional contact-based strain-gauge sensors.

Table VIII provides a comparison between the proposed sensor, other research-based sensors, and commercially available six-axis force/torque sensors. The proposed sensor demonstrates superior accuracy compared to magnetic and pressure-based sensors while also achieving the highest resolution among all compared systems. Moreover, with a sampling rate of 4 kHz, it operates significantly faster than typical commercial sensors.

The proposed system supports a maximum sampling rate of approximately 4 kHz, which is the upper limit defined by the LDC1614 hardware specifications. However, in the static and comparative experiments conducted in this study, a sampling rate of 1 kHz was employed to ensure compatibility with the reference sensor and maintain signal stability.

The proposed sensor is based on inductive sensing and utilizes a non-contact measurement approach. It employs only six sensing elements, which is relatively low compared to other configurations. Sensors developed using photocouplers or capacitive principles are generally optimized for miniaturization. In contrast, strain-gauge-based sensors tend to be bulky and require a minimum of 12 strain-gauges to measure six degrees of freedom. Magnetic and pressure-based sensors typically suffer from low resolution and poor accuracy. The system's compact design, non-contact operation, and integrated high-speed signal processing unit highlight its suitability for embedded robotic applications.

While the proposed sensor currently employs inductive sensing, its performance is still limited by non-optimized parameters such as the number of coil turns, the number of layers, and the distance to the conductive target. These factors represent the current limitations of this study. For example, the horizontal sensing coils—which are responsible for measuring the  $x$ - and  $y$ -axis forces and the  $z$ -axis torque—currently exhibit higher resolution than the vertical sensing coils, which measure the  $x$ - and  $y$ -axis torques and the  $z$ -axis force. This discrepancy suggests that further optimization of the coil turns and the distance to the target could lead to improved performance in all measurement axes.

As future work, performance is expected to improve through optimization of the coil turns, layer configuration, and spacing to the conductive target. Additionally, temperature compensation will be incorporated to further enhance sensor robustness under varying environmental conditions. In addition, further investigation is required to assess the sensor's robustness in electromagnetic interference (EMI) and electromagnetic compatibility (EMC) environments. Due to the nature of inductive sensing, the system may be susceptible to electromagnetic disturbances. Therefore, comprehensive stability testing and the implementation of shielding strategies in the design should be considered to ensure reliable operation under such conditions. While a formal sensitivity analysis of the nonlinear fitting function is not included, the system demonstrated reliable performance under various test conditions. More detailed



TABLE VIII  
COMPARISON WITH OTHER F/T SENSORS

	Accuracy(FSE(%))	Sampling Rate	Resolution	Contact
<b>Proposed Method</b>	1.0	~4,000Hz	15-bit w/o external DAQ	Non-contact
Optical type [18]	2.0	5,000 Hz	14-bit w/o external DAQ	Non-contact
Capacitor type [10]	4.1	200 Hz	11-bit w/o external DAQ	Non-contact
Magnetic type [27]	22.5	2 ms delay	low	Non-contact
Pressure Sensing type [17]	22.2	1,000 Hz	Low	Contact
RFT80-6A01(Commercial) [28]	3.0	1,000 Hz	13-bit w/o external DAQ	Non-contact
AFT200-KIT(Commercial) [26]	-	1,000 Hz	11-bit w/o external DAQ	Non-contact
SensOne-Serial(Commercial) [29]	2.0	800 Hz	11-bit w/o external DAQ	Contact
MINI-85(Commercial) [7]	~ 2.0	7,000 Hz	13-bit with DAQ	Contact
	Weight	Load Capacity	Number of Sensors	Sensing Method
<b>Proposed Method</b>	280g	2,870 N	6	Inductive Sensor
Optical type [18]	79 g	3,700 N	6	Photocoupler
Capacitor type [10]	15 g	100 N	6	Capacitive Sensor
Magnetic type [27]	-	1,000 N	5(2DOF)	Magnetic Sensor
Pressure Sensing type [17]	-	450 N~	9(3DOF)	Pressure Sensor
RFT80-6A01(Commercial) [28]	226 g	800 N	6	Capacitive Sensor
AFT200-KIT(Commercial) [26]	236 g	400 N	6	Capacitive Sensor
SensOne-Serial(Commercial) [29]	235 g	2,400 N	12	Strain-gauge
MINI-85(Commercial) [7]	635 g	3,800 N	12	Strain-gauge

noise analysis could be a topic for future exploration if the calibration method is further generalized or applied to different sensor platforms.

## REFERENCES

- [1] J. Di Carlo, P. M. Wensing, B. Katz, G. Bledt, and S. Kim, "Dynamic locomotion in the mit cheetah 3 through convex model-predictive control," in *2018 IEEE/RSJ international conference on intelligent robots and systems (IROS)*, pp. 1–9. IEEE, 2018.
- [2] S. Choi, G. Ji, J. Park, H. Kim, J. Mun, J. H. Lee, and J. Hwangbo, "Learning quadrupedal locomotion on deformable terrain," *Science Robotics*, vol. 8, no. 74, p. eade2256, 2023.
- [3] J. Kang, H. Kim, and K.-S. Kim, "View: Visual-inertial external wrench estimator for legged robot," *IEEE Robotics and Automation Letters*, vol. 8, no. 12, pp. 8366–8373, 2023.
- [4] G. Valsecchi, R. Grandia, and M. Hutter, "Quadrupedal locomotion on uneven terrain with sensorized feet," *IEEE Robotics and Automation Letters*, vol. 5, no. 2, pp. 1548–1555, 2020.
- [5] Y. Liu, S. Liu, B. Chen, Z.-X. Yang, and S. Xu, "Fusion-perception-to-action transformer: Enhancing robotic manipulation with 3d visual fusion attention and proprioception," *IEEE Transactions on Robotics*, 2025.
- [6] J. Chen, Z.-Y. Dong, S. Shi, Y. Wei, X. Yu, and L. Ou, "Adaptive-constrained admittance control for physical human-robot interaction," *Transactions of the Institute of Measurement and Control*, p. 01423312241298351, 2025.
- [7] "Ati industrial automation," <https://www.ati-ia.com/>, accessed: 2025-05-14.
- [8] J.-H. Kim, "Multi-axis force-torque sensors for measuring zero-moment point in humanoid robots: A review," *IEEE Sensors Journal*, vol. 20, no. 3, pp. 1126–1141, 2019.
- [9] P. Billeschou, C. Albertsen, J. C. Larsen, and P. Manoonpong, "A low-cost, compact, sealed, three-axis force/torque sensor for walking robots," *IEEE Sensors Journal*, vol. 21, no. 7, pp. 8916–8926, 2021.
- [10] U. Kim, D.-H. Lee, Y. B. Kim, D.-Y. Seok, and H. R. Choi, "A novel six-axis force/torque sensor for robotic applications," *IEEE/ASME Transactions on mechatronics*, vol. 22, no. 3, pp. 1381–1391, 2016.
- [11] M. Pu, Q. Luo, Q. Liang, and J. Zhang, "Modeling for elastomer displacement analysis of capacitive six-axis force/torque sensor," *IEEE Sensors Journal*, vol. 22, no. 2, pp. 1356–1365, 2021.
- [12] Q. Luo, Q. Liang, J. Zhang, R. Zhao, Z. Ai, and M. Pu, "Parameters optimization for a capacitive six-axis force/torque sensor by using analytical method," *IEEE Sensors Journal*, vol. 22, no. 22, pp. 21 735–21 744, 2022.
- [13] U. Kim, Y. B. Kim, D.-Y. Seok, J. So, and H. R. Choi, "A surgical palpation probe with 6-axis force/torque sensing capability for minimally invasive surgery," *IEEE Transactions on Industrial Electronics*, vol. 65, no. 3, pp. 2755–2765, 2017.
- [14] U. Kim, Y. B. Kim, J. So, D.-Y. Seok, and H. R. Choi, "Sensorized surgical forceps for robotic-assisted minimally invasive surgery," *IEEE Transactions on Industrial Electronics*, vol. 65, no. 12, pp. 9604–9613, 2018.
- [15] G. Palli and S. Pirozzi, "An optical torque sensor for robotic applications," *International Journal of Optomechatronics*, vol. 7, no. 4, pp. 263–282, 2013.
- [16] O. Al-Mai, M. Ahmadi, and J. Albert, "Design, development and calibration of a lightweight, compliant six-axis optical force/torque sensor," *IEEE Sensors Journal*, vol. 18, no. 17, pp. 7005–7014, 2018.
- [17] Á. Tar and G. Cserey, "Development of a low cost 3d optical compliant tactile force sensor," in *2011 IEEE/ASME International Conference on Advanced Intelligent Mechatronics (AIM)*, pp. 236–240. IEEE, 2011.
- [18] H.-B. Kim, K.-H. Choi, and K.-S. Kim, "A compact six-axis force/torque sensor using photocouplers for impact robustness," *Review of Scientific Instruments*, vol. 95, no. 4, 2024.
- [19] S. Jeong, Y. Chitalia, and J. P. Desai, "Miniature force sensor based on dual-photointerrupter with high linearity and disturbance compensation," *IEEE Sensors Journal*, vol. 20, no. 11, pp. 5855–5864, 2020.
- [20] S. H. Jeong, H. J. Lee, K.-R. Kim, and K.-S. Kim, "Design of a miniature force sensor based on photointerrupter for robotic hand," *Sensors and Actuators A: Physical*, vol. 269, pp. 444–453, 2018.
- [21] L. Xiong, Y. Guo, G. Jiang, X. Zhou, L. Jiang, and H. Liu, "Six-dimensional force/torque sensor based on fiber bragg gratings with low coupling," *IEEE Transactions on Industrial Electronics*, vol. 68, no. 5, pp. 4079–4089, 2020.
- [22] H.-P. Wang, J.-G. Dai, and X.-Z. Wang, "Improved temperature compensation of fiber bragg grating-based sensors applied to structures under different loading conditions," *Optical Fiber Technology*, vol. 63, p. 102506, 2021.
- [23] F. W. Grover, *Inductance calculations: working formulas and tables*. Courier Corporation, 2004.
- [24] S. S. Mohan, M. del Mar Hershenson, S. P. Boyd, and T. H. Lee, "Simple accurate expressions for planar spiral inductances," *IEEE Journal of solid-state circuits*, vol. 34, no. 10, pp. 1419–1424, 1999.
- [25] "Texas instruments application note(snoa930a)," <https://www.ti.com/lit/an/snoa930a/snoa930a.pdf>, accessed: 2025-05-14.
- [26] "Aidinrobotics," <https://www.aidinrobotics.co.kr/smart-6-axis-f-t-sensor>, accessed: 2025-05-14.
- [27] A. Ananthanarayanan, S. Foong, and S. Kim, "A compact two dof magneto-elastomeric force sensor for a running quadruped," in *2012 IEEE International Conference on Robotics and Automation*, pp. 1398–1403. IEEE, 2012.
- [28] "Robotous - innovative robotic solutions," <http://www.robotous.com/main>, accessed: 2025-05-14.
- [29] "Bota systems," <https://www.botasys.com/>, accessed: 2025-05-14.



**Hyun-Bin Kim** obtained his B.S., M.S., and Ph.D. degrees in Mechanical Engineering from Korea Advanced Institute of Science and Technology (KAIST), Daejeon, Republic of Korea, in 2020, 2022, and 2025 respectively. Currently serving as a post-doctoral researcher at KAIST, his current research interests include force/torque sensors, legged robot control, robot design, and mechatronics systems.



Technology.

**Kyung-Soo Kim** (Fellow, IEEE) obtained his B.S., M.S., and Ph.D. degrees in Mechanical Engineering from Korea Advanced Institute of Science and Technology (KAIST), Daejeon, Republic of Korea, in 1993, 1995, and 1999, respectively. Since 2007, he has been with the Department of Mechanical Engineering, KAIST. His research interests include control theory, electric vehicles, and autonomous vehicles. He serves as an Associate Editor for the *Automatica* and the *Journal of Mechanical Science and*